Ferroelectric Properties and Ambipolar Carrier Transport of 9-Fluorenone–Based Liquid Crystals

Sou-un Doi , Syota Yamada , Ken'ichi Aoki , Atsushi Seki *

Posted Date: 6 November 2025

doi: 10.20944/preprints202511.0407.v1

Keywords: chiral liquid crystals; ferroelectricity; carrier transport

Article

Ferroelectric Properties and Ambipolar Carrier Transport of 9-Fluorenone–Based Liquid Crystals

Sou-un Doi [1], Syota Yamada [1], Ken'ichi Aoki [1,2] and Atsushi Seki [1,2,3,*]

[1] Department of Chemistry, Graduate School of Science, Tokyo University of Science, 1-3 Kagurazaka, Shinjuku-ku, Tokyo 162-8601, Japan

[2] Department of Chemistry, Faculty of Science Division II, Tokyo University of Science, 1-3 Kagurazaka, Shinjuku-ku, Tokyo 162-8601, Japan

[3] Material and Biological Engineering Course, Department of Industrial Systems Engineering, National Institute of Technology (KOSEN), Hachinohe College, 16-1 Uwanotai, Tamonoki, Hachinohe, Aomori 039-1192, Japan

* Correspondence: a_seki_3@rs.tus.ac.jp or aseki-c@hachinohe.kosen-ac.jp; Tel.: +81-178-27-7289

Abstract

The functional integration of chiral liquid crystals and π-conjugated compounds has great potential for creating novel exotic materials. We synthesized a series of chiral donor–acceptor (D–A)-type fluorenone derivatives to investigate the influence of molecular structure upon their phase-transition behavior, ferroelectricity, and photophysical and photoconductive properties. Polarizing optical microscopy and differential scanning calorimetry analyses revealed that several D–A-type fluorenone derivatives exhibited liquid crystal (LC) phases. These chiral LC fluorenone derivatives exhibited polarization hysteresis behavior in the chiral smectic C (SmC*) phase. Among the four ferroelectric liquid-crystalline fluorenone derivatives, (*R*,*R*)-**2a** exhibited the largest spontaneous polarization (over 3.0×10^2 nC cm^{-2}). The formation of intramolecular charge-transfer states in each compound was evidenced in the UV–vis absorption spectra. Using the time-of-flight method, the ambipolar carrier transport in the SmC* phases of the fluorenone-based LCs was clarified. The hole and electron mobilities in the SmC* phases were on the order of 10^{-5} cm^2 V^{-1} s^{-1}, which is on par with the carrier mobilities of low-ordered smectic phases in conventional LC semiconductors.

Keywords: chiral liquid crystals; ferroelectricity; carrier transport

1. Introduction

Chiral molecular assemblies exhibit characteristic properties absent in the achiral counterparts [1 – 8]. The hierarchical suprastructures reflecting molecular chirality offer platforms for biopharmacological, chemical, and physical functions [1–8]. While helical self-assembly is the most common chiral supramolecular system, molecular chirality often triggers the formation of broken-symmetry aggregated structures. Because the symmetry reduction of self-organized structures results in the stabilization of polar structures, ferroelectric behavior is observed in some chiral suprastructures [9–11]. The incorporation of molecular chirality contributes to the manifestation of various unique integrated functionalities [12,13]. Thus, various chiral soft materials such as chiral liquid crystals (CLCs) [6–8], chiral polymers [4,14,15], and chiral supramolecular polymers [15,16] have been extensively developed and studied. Remarkably, CLCs exhibit high responsivity to external stimuli, such as temperature and electric fields, owing to their dynamic features [7,8]. In the past decade, we have paid attention to chiral smectic liquid crystals forming polar structures [17–22]. The most classical ferroelectric liquid crystal (FLC) is a CLC that exhibits a chiral smectic C (SmC*)

 doi:10.20944/preprints202511.0407.v1

phase [9,10]. Conventional CLCs have generally been studied for applications in optical sensors [23] and high-speed LC displays [24].

Aromatic compounds, including oligoacenes [25] and oligothiophenes [26], have been widely studied as organic semiconductors owing to their structural diversity, favorable processability, and good carrier-transport properties in condensed states [27–30]. LC compounds integrating a planar aromatic mesogenic core can be regarded as semiconductors. In the past few decades, the anisotropic conduction of electronic charge carriers in LC structures has been deeply discussed [31–36]. The transport of both positive and negative carriers in various LC phases has also been extensively studied [37–44]. Furthermore, LC semiconductors have been applied in lightweight and flexible organic electronic devices such as thin-film field-effect transistors [45–48], light-emitting diodes [49–51], and solar cells [52,53].

Whereas typical CLCs are insulators, CLCs with extended π-conjugated cores exhibit electronic carrier transport [17–22, 54–57]. These chiral π-conjugated LCs have the potential to create novel function-integrated materials. For example, ferroelectric π-conjugated LCs exhibiting a bulk photovoltaic effect (BPVE) have been developed [17,20,22]. The BPVE in LC phases results from the coupling effect of spontaneous polarization and carrier transport [18]. The BPVE, one of the bandgap-independent photovoltaic effects, clearly differs from classical photovoltaic effects based on p-n junctions. Therefore, the development of materials incorporating CLCs is important.

Thermally stable fluorenone is an easily modified rigid electron acceptor unit with a planar π-conjugated system [58–60]. The central carbonyl moiety is a polar group, which can contribute to the enhancement of spontaneous polarization. The incorporation of donor units onto fluorenone can cause intramolecular charge transfer, which results in the formation of local electrical polarization as well as the appearance of a broad light-absorption band in the long-wavelength range [61,62]. In addition, some LC donor–acceptor (D–A)-type fluorenone derivatives exhibit good carrier-transport properties [59].

In this study, a series of fluorenone derivatives incorporating chiral moieties was synthesized (Figure 1). After basic characterization of the LC properties, the electrostatic and electronic charge-carrier transport properties of the chiral fluorenone derivatives were studied.

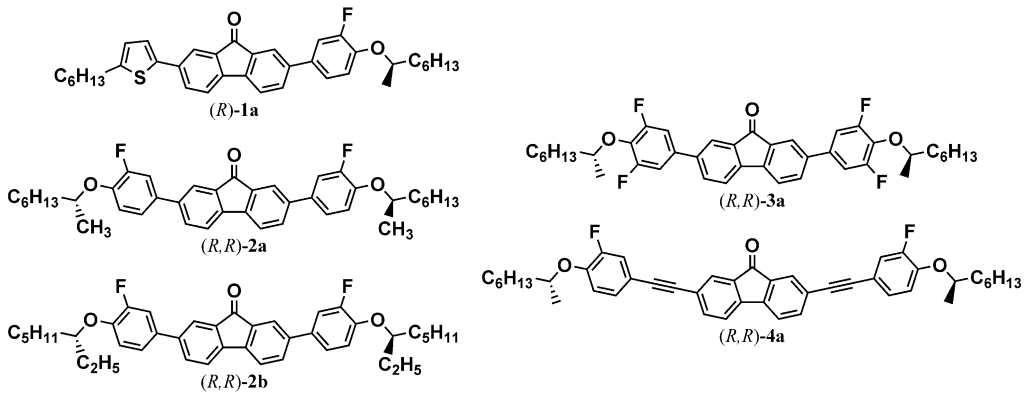

Figure 1. Chemical structures of the chiral fluorenone derivatives.

2. Materials and Methods

2.1. General Procedures and Materials

All chemical reagents were purchased from FUJIFILM Wako Pure Chemical (Osaka, Japan), Kanto Chemicals (Tokyo, Japan), and Tokyo Chemical Industry (Tokyo, Japan) and used without further purification. All reactions were performed under an argon atmosphere in a well-dried flask equipped with a magnetic stirring bar. All ^{1}H and ^{13}C NMR spectra were acquired using a Bruker

 doi:10.20944/preprints202511.0407.v1

(Osaka, Japan) Biospin AVANCE NEO 400 spectrometer (400 MHz for ^{1}H NMR spectra, 100 MHz for ^{13}C NMR spectra). All chemical shifts (δ) in the ^{1}H and ^{13}C NMR spectra are quoted in ppm. Tetramethylsilane of 0.03 vol% was used as the internal standard to determine δ = 0.00 ppm. High-resolution mass spectrometry (HRMS) measurements were performed by electrospray ionization (ESI) using a SCIEX (Tokyo, Japan) X500R QTOF spectrometer.

2.2. Synthesis and Characterization of Target Compounds

A scheme and details of the synthesis of the target compounds are given in the attached Supplementary Files (Section S2.1. Synthesis).

2.2.1. Characterization of (R)-1a

^{1}H NMR (400 MHz, $CDCl_3$): δ [ppm] = 7.85 (dd, *J* = 10.0, 1.3 Hz, 2H), 7.69–7.62 (m, 2H), 7.53 (d, *J* = 7.7 Hz, 1H), 7.49 (d, *J* = 7.8 Hz, 1H), 7.35 (dd, *J* = 12.3, 2.2 Hz, 1H), 7.32–7.29 (m, 1H), 7.20 (d, *J* = 3.6 Hz, 1H), 7.03 (t, *J* = 8.5 Hz, 1H), 6.77 (d, *J* = 3.6 Hz, 1H), 4.41 (sextet, *J* = 6.1 Hz, 1H), 2.83 (t, *J* = 7.5 Hz, 2H), 1.88–1.57 (m, 4H), 1.52–1.25 (m, 17H), 0.95–0.84 (m, 6H); ^{13}C-NMR (100 MHz, $CDCl_3$) : δ [ppm] = 193.6, 153.8 (d, *J* = 244.7 Hz), 146.7, 146.1 (d, *J* = 10.7 Hz), 143.0, 142.3, 140.6 (d, *J* = 1.6 Hz), 140.3, 135.8, 135.2, 133.1 (d, *J* = 6.5 Hz), 132.7, 131.2, 125.3, 123.4, 122.5, 122.4 (d, *J* = 3.1 Hz), 121.1, 120.8, 120.7, 117.6 (d, *J* = 2.2 Hz), 114.7 (d, *J* = 20.2 Hz), 76.4, 36.5, 31.8, 31.6, 30.3, 29.3, 28.8, 25.5, 22.6, 22.6, 19.9, 14.1; HRMS (ESI): molecular weight ($C_{37}H_{41}FO_2S$) = 568.2811; *m*/*z* calcd. for $[C_{37}H_{42}FO_2S]^+$ ($[M + H]^+$) = 569.2884; *m*/*z* found = 569.2878.

2.2.2. Characterization of (R,R)-2a

^{1}H NMR (400 MHz, $CDCl_3$): δ [ppm] = 7.85 (d, *J* = 1.3 Hz, 2H), 7.66 (dd, *J* = 7.7, 1.7 Hz, 2H), 7.57 (d, *J* = 7.8 Hz, 2H), 7.36 (dd, *J* = 12.2, 2.2 Hz, 2H), 7.33–7.29 (m, 2H), 7.04 (t, *J* = 8.5 Hz, 2H), 4.41 (sextet, *J* = 6.1 Hz, 2H), 1.89–1.73 (m, 2H), 1.69–1.57 (m, 2H), 1.52–1.24 (m, 22H), 0.89 (t, *J* = 6.9 Hz, 6H); ^{13}C-NMR (100 MHz, $CDCl_3$) : δ [ppm] = 193.6, 153.8 (d, *J* = 244.4 Hz), 146.1 (d, *J* = 10.8 Hz), 142.8, 140.7 (d, *J* = 1.8 Hz), 135.2, 133.0 (d, *J* = 6.7 Hz), 132.7, 122.5, 122.4 (d, *J* = 3.4 Hz), 120.8, 117.6 (d, *J* = 2.2 Hz), 114.7 (d, *J* = 19.7 Hz), 76.4, 36.5, 31.8, 29.3, 25.5, 22.6, 19.8, 14.1; HRMS (ESI): molecular weight ($C_{41}H_{46}F_2O_3$) = 624.3415; *m*/*z* calcd. for $[C_{41}H_{47}F_2O_3]^+$ ($[M + H]^+$) = 625.3488; *m*/*z* found = 625.3486.

2.2.3. Characterization of (R,R)-2b

^{1}H NMR (400 MHz, $CDCl_3$): δ [ppm] = 7.85 (d, *J* = 1.4 Hz, 2H), 7.66 (dd, *J* = 7.8, 1.8 Hz, 2H), 7.56 (d, *J* = 7.7 Hz, 2H), 7.35 (dd, *J* = 12.3, 2.3 Hz, 2H), 7.33–7.28 (m, 2H), 7.04 (t, *J* = 8.6 Hz, 2H), 4.24 (quintet, *J* = 5.9 Hz, 2H), 1.80–1.61 (m, 8H), 1.53–1.24 (m, 12H), 1.00 (t, *J* = 7.4 Hz, 6H), 0.89 (t, *J* = 7.0 Hz, 6H); ^{13}C-NMR (100 MHz, $CDCl_3$) : δ [ppm] = 193.6, 153.7 (d, *J* = 244.7 Hz), 146.6 (d, *J* = 10.8 Hz), 142.8, 140.8 (d, *J* = 2.0 Hz), 135.2, 132.9 (d, *J* = 6.5 Hz), 132.7, 122.5, 122.4 (d, *J* = 3.4 Hz), 120.8, 117.5 (d, *J* = 2.5 Hz), 114.8 (d, *J* = 19.7 Hz), 81.5, 33.4, 31.9, 26.6, 25.0, 22.6, 14.0, 9.5; HRMS (ESI): molecular weight ($C_{41}H_{46}F_2O_3$) = 624.3415; *m*/*z* calcd. for $[C_{41}H_{47}F_2O_3]^+$ ($[M + H]^+$) = 625.3488; *m*/*z* found = 625.3488.

2.2.5. Characterization of (R,R)-3a

^{1}H NMR (400 MHz, $CDCl_3$): δ [ppm] = 7.81 (d, *J* = 1.4 Hz, 2H), 7.65 (dd, *J* = 7.8, 1.8 Hz, 2H), 7.58 (d, *J* = 7.8 Hz, 2H), 7.15 (d, *J* = 9.1 Hz, 4H), 4.34 (sextet, *J* = 6.1 Hz, 2H), 1.87–1.72 (m, 2H), 1.67–1.57 (m, 2H), 1.56–1.23 (m, 22 H), 0.89 (t, *J* = 6.8 Hz, 6H); ^{13}C-NMR (100 MHz, $CDCl_3$) : δ [ppm] = 193.0, 156.8 (dd, *J* = 246.9, 6.5 Hz), 143.3, 139.9, 135.3, 134.6 (d, *J* = 17.7 Hz), 134.6 (d, *J* = 14.4 Hz), 134.4, 132.9, 122.6, 121.0, 110.3 (dd, *J* = 16.8, 7.0 Hz), 81.2, 36.9, 31.8, 29.3, 25.3, 22.6, 20.1, 14.1 ; HRMS (ESI): molecular weight ($C_{41}H_{44}F_4O_3$) = 660.3227; *m*/*z* calcd. for $[C_{41}H_{45}F_4O_3]^+$ ($[M + H]^+$) = 661.3299; *m*/*z* found = 661.3298.

2.2.6. Characterization of (R,R)-4a

^{1}H NMR (400 MHz, $CDCl_3$): δ [ppm] = 7.76 (d, *J* = 1.5 Hz, 2H), 7.61 (dd, *J* = 7.7, 1.5 Hz, 2H), 7.49 (d, *J* = 7.7 Hz, 2H), 7.28–7.19 (m, 4H), 6.92 (t, *J* = 8.7 Hz, 2H), 4.40 (sextet, *J* = 6.1 Hz, 2H), 1.87–1.71 (m,

 doi:10.20944/preprints202511.0407.v1

2H), 1.66–1.55 (m, 2H), 1.52–1.22 (m, 22H), 0.89 (t, J = 6.9 Hz, 6H) ; ^{13}C NMR (100 MHz, $CDCl_3$): δ [ppm] = 192.2, 152.9 (d, J = 244.7 Hz), 147.1 (d, J = 10.3 Hz), 143.1, 137.7, 134.4, 128.2 (d, J = 3.4 Hz), 127.3, 124.4, 120.6, 119.5 (d, J = 20.2 Hz), 116.7 (d, J = 2.5 Hz), 115.2 (d, J = 8.5 Hz), 90.5 (d, J = 2.7 Hz), 87.9, 76.3, 36.4, 31.8, 29.2, 25.4, 22.6, 19.8, 14.1; HRMS (ESI): molecular weight ($C_{45}H_{46}F_2O_3$) = 672.3415; m/z calcd. for $[C_{45}H_{47}F_2O_3]^+$ ($[M + H]^+$) = 673.3488; m/z found = 673.3484.

2.3. Characterization of Light-Absorption Properties

UV–vis absorption spectra were obtained using a JEOL V-650 spectrometer. The absorption spectra of dilute solutions (10 μM) were measured using a pair of quartz cells with a cell path length of 1 cm. The absorption spectra in the bulk state were measured using the sample-filled ITO sandwich cells (cell gap: 2 μm).

2.4. Characterization of LC Properties

The LC properties of each compound were studied using polarizing optical microscopy (POM), differential scanning calorimetry (DSC), and X-ray diffraction (XRD). The optical texture was observed using a polarizing optical microscope (Olympus BH2, Olympus Corporation, Tokyo, Japan) equipped with a temperature control system (METTLER TOLEDO FP90 and FP82HT) and a digital camera (AS ONE HDCE-X1, AS ONE Corporation, Osaka, Japan). Indium tin oxide (ITO) sandwich cells filled with chiral π-conjugated compounds were used for POM observations. Empty ITO sandwich cells (KSSO-02/A311P1NSS05, cell gap: 2 μm) were purchased from EHC Corporation (Tokyo, Japan). The polyimide-free ITO surface was rubbed to facilitate planar orientation of the LC phases. DSC measurements were conducted using a SHIMADZU (Kyoto, Japan) DSC-60 system equipped with a liquid nitrogen auto-cooling system (TAC-60L). Approximately 2–3 mg of each sample was sealed in an aluminum pan. The scan rate for the POM and DSC measurements was 10 °C min^{-1}. XRD analysis was performed using a Rigaku Miniflex (Ni-filtered Cu Kα radiation, Rigaku Corporation, Tokyo, Japan) equipped with a thermal control system.

3. Results and Discussion

3.1. Light-Absorption Properties

Figure 2a shows the UV–vis absorption spectra of (*R*)-**1a**, (*R*,*R*)-**2a**, (*R*,*R*)-**3a**, and (*R*,*R*)-**4a** in tetrahydrofuran (10 μM). In the absorption spectra of each compound, several strong absorption peaks appeared in the range of 290–360 nm, with a weak, broad absorption band spanning 400 to 550 nm. While the intense absorption bands in the short wavelength range (high energy region) contribute to local excitation of the central aromatic core, the broad absorption band from 400 to 550 nm is probably attributed to an intramolecular charge transfer (ICT) transition. Among the four compounds, (*R*,*R*)-**4a** showed the largest molar coefficient of the ICT absorption band. A similar enhancement of the molar coefficient upon insertion of an ethynyl linker between electron-deficient fluorenone and phenyl rings was reported for the analogous D–A–D-type fluorenone derivatives [63]. Among the solutions of the four D–A–D-type fluorenone derivatives, the THF solution of (*R*)-**1a** exhibited the lowest absorption edge energy in the UV–vis absorption spectrum. The substitution of the electron-rich thiophene moiety probably stabilized the ICT excited state and narrowed the gap between the ICT ground and excited states. Among the film samples of (*R*)-**1a**, (*R*,*R*)-**2a**, (*R*,*R*)-**3a**, and (*R*,*R*)-**4a**, the LC film of (*R*)-**1a** covered the widest range in the visible light region of the UV–vis absorption spectrum, due to the molecular alignment in the LC cell, and planarity of π-conjugated unit in the aggregated state (Figure 2b).

 doi:10.20944/preprints202511.0407.v1

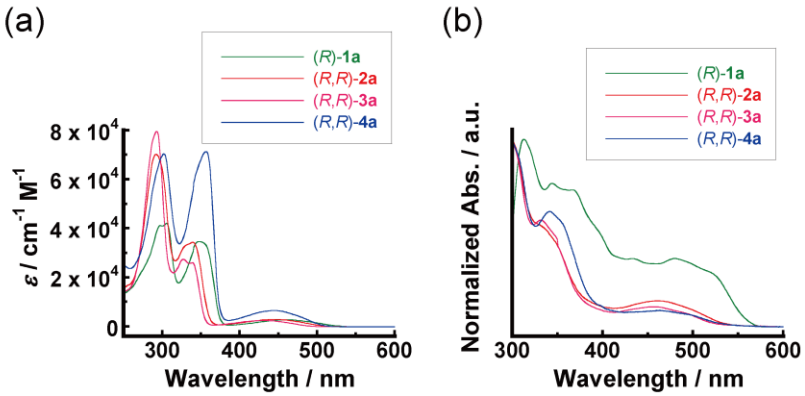

Figure 2. UV–vis absorption spectra of chiral fluorenone derivatives (a) in THF solution (10 μM) and of (b) bulk sample at room temperature in a 2 μm thick cell.

3.2. Liquid-Crystalline Properties

3.2.1. Polarizing Optical Microscopy

In the POM analysis of chiral fluorenone derivative (*R*)-**1a**, a fan-shaped texture was observed at ~185 °C on cooling from the isotropic liquid (IL) state (Figure 3a). The characteristic broken-fan-shaped domains indicate the formation of a tilted-layer structure in the chiral smectic C (SmC*) phase. By contrast, a complex optical texture with many disclination lines was observed at 90 °C (Figure 3b). The apparent change in optical texture indicated a phase transition from SmC* to ordered smectic phases. The complicated texture in the ordered phase (Figure 3b) was retained without conspicuous domain shape changes upon further cooling to room temperature. The POM analysis of (*R,R*)-**2a** implied that the chiral 2,7-disubstituted fluorenone derivative exhibited several LC phases during cooling from the IL phase (Figure 4a–c). The characteristic fan-shaped texture of the smectic phase appeared at 153 °C upon cooling from the IL phase (Figure 4a). The fan-shaped domain with smooth interfaces indicated the presence of the chiral smectic A (SmA*) phase. After the sample cooled to 135 °C, the distinctive fan-shaped domains were observed (Figure 4b). Furthermore, a textural change owing to the phase transition was evident at ~50 °C (Figure 4c). By contrast, (*R,R*)-**2b** was a clear viscous liquid at room temperature. In the POM study of (*R,R*)-**2b**, the image appeared dark and homogeneous owing to the lack of birefringence above room temperature. Upon cooling from the IL phase of (*R,R*)-**3a**, the fan-shaped texture was observed at 170 °C (Figure 5a). When the sample cooled to ~130 °C, the stripes in the fan-like domains became prominent (Figure 5b). Considering the phase transition sequence, the high- and low-temperature LC phases should be SmA* and SmC* phases, respectively. A more explicit optical textural change was observed below 95 °C, during the cooling process (Figure 5c). (*R,R*)-**4a** formed broken-fan-like domains at 95 °C (Figure 6a). The domain shapes were mostly retained after cooling to 65 °C (Figure 6b).

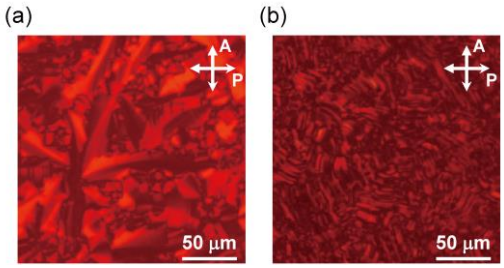

Figure 3. POM images of (*R*)-**1a** at (a) 185 °C and (b) 90 °C upon cooling.

 doi:10.20944/preprints202511.0407.v1

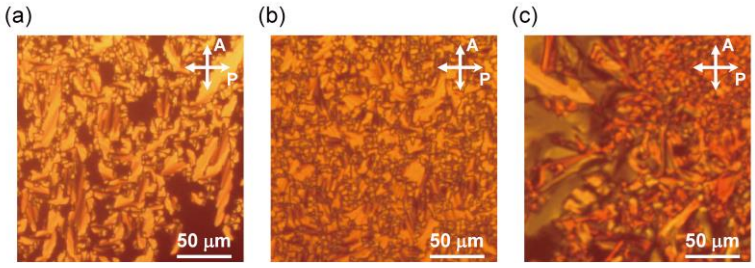

Figure 4. POM images of (*R*,*R*)-**2a** at (a) 153 °C, (b) 135 °C, and (c) 50 °C upon cooling.

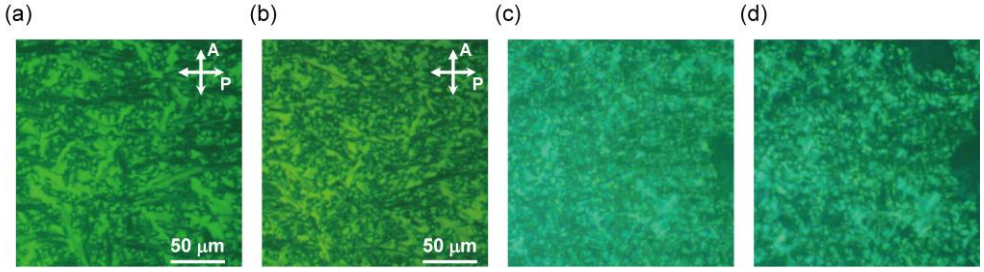

Figure 5. POM images of (*R*,*R*)-**3a** at (a) 170 °C, (b) 130 °C, and (c) 50 °C upon cooling.

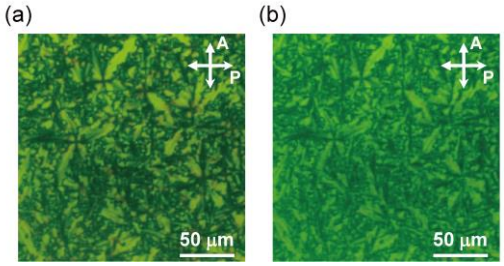

Figure 6. POM images of (*R*,*R*)-**4a** at (a) 95 °C, and (b) 65 °C upon cooling.

3.2.2. Differential Scanning Calorimetry

In the DSC thermogram of (*R*)-**1a**, two endothermic peaks of phase transitions appear during the second heating scan (Figure 7a). The first peak at 109 °C corresponds to the transition from an ordered phase to the SmC* phase. The transition enthalpy of 11 kJ mol^{-1} is almost equal to that of the ordered smectic-SmC* phase transition in other systems [18,21]. The transition from SmC* to IL phases gives rise to a second peak at 192 °C, which is the clearing temperature. The DSC thermogram of (*R*,*R*)-**2a** reveals three endothermic peaks during the second heating process (Figure 7b). The peak at 77 °C indicates an ordered smectic-SmC* phase transition, while the second small peak at 140 °C represents the SmC*–SmA* phase transition. (*R*,*R*)-**2a** exhibits the SmA* phase between 140 °C and 156 °C. Notably, no endothermic peaks corresponding to first-order phase transitions are apparent in the DSC thermogram of (*R*,*R*)-**2b**. The DSC study also indicates that (*R*,*R*)-**2b** is not an LC. Among the five compounds, (*R*,*R*)-**3a** shows the most complex phase-transition behavior. A few peaks appeared below 90 °C in the DSC thermogram of (*R*,*R*)-**3a** (Figure 7c). These peaks imply gradual disruption of the intralayer bond order in the ordered smectic phase. (*R*,*R*)-**3a** exhibits the ordered smectic-SmC* phase transition at ~100 °C. Subsequently, the SmC*–SmA* phase transition occurs at 137 °C. The relatively stable SmA* phase was retained at ~180 °C. (*R*,*R*)-**4a** bearing a rigid ethynyl-bridged D–A core exhibits a crystalline (Cr) phase at room temperature. The Cr phase was transformed into the SmC* phase at 92 °C, which was retained below the clearing temperature of 127 °C (Figure 7d).

 doi:10.20944/preprints202511.0407.v1

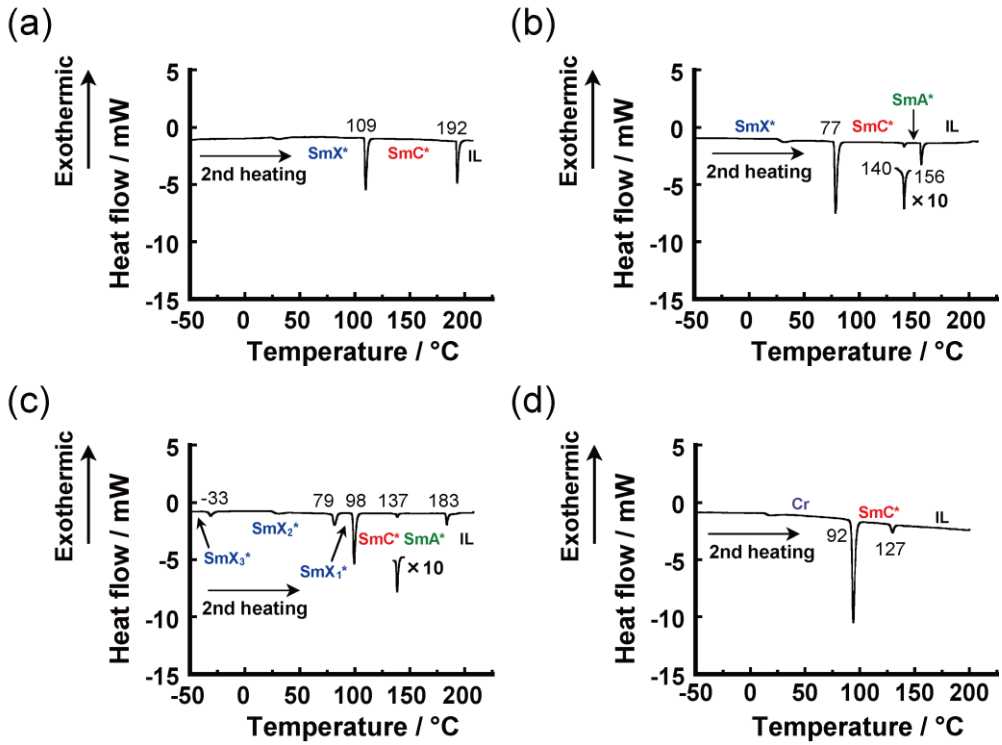

Figure 7. DSC thermograms of (a) (*R*)-**1a**, (b) (*R*,*R*)-**2a**, (c) (*R*,*R*)-**3a**, and (d) (*R*,*R*)-**4a** at a scan rate of 10 °C min^{-1}.

The thermal phase-transition behaviors of fluorenone derivatives are summarized in Table 1. While the fluorenone derivative (*R*,*R*)-**2b** is not an LC, the other four compounds exhibit an enantiotropic SmC* phase. Notably, direct modification with donor units on both wings of the fluorenone core stabilizes the SmA* phase. The asymmetrically modified fluorenone derivative (*R*)-**1a** exhibited the highest clearing temperature among the four LC fluorenone derivatives. Analysis of the UV–vis absorption spectra (Section 3.1, Figure 2) indicated that the π-conjugated system was well-developed owing to the higher planarity of the rigid aromatic core in compound (*R*)-**1a** among the five chiral fluorenone derivatives. In addition, the free volume of motile side chains in (*R*)-**1a** would be smaller than the other compounds when the molecular structure is considered. Thus, the weak dynamic effect that disturbs the molecular packing and enhances intermolecular interactions between the central cores resulted in the high clearing temperature of (*R*)-**1a**. In the case of (*R*,*R*)-**2b**, the steric and dynamic effects of the bulky, chiral branched alkyl chain interfered with aggregation and thus reduced the liquid crystallinity.

Table 1. Phase-transition behavior of chiral fluorenone derivatives.

Compound	Phase Transition Temperature / °C (Enthalpy / kJ mol^{-1}) [1,2]
(*R*)-**1a**	SmX* 109 (11) SmC* 192 (8) IL
(*R*,*R*)-**2a**	SmX$_1$* 77 (16) SmC* 140 (1) SmA* 156 (3) IL
(*R*,*R*)-**2b**	G 44 IL
(*R*,*R*)-**3a**	SmX$_3$* –33 (2) SmX$_2$* 79 (4) SmX$_1$* 98 (11) SmC* 137 (1) SmA* 183 (2) IL
(*R*,*R*)-**4a**	Cr 92 (23) SmC* 127 (2) IL

[1] The phase transition temperature and enthalpy were estimated from the second heating scans of DSC thermograms. [2] Cr, IL, SmA*, and SmC* denote the crystal, isotropic liquid, chiral smectic A, and chiral smectic C phases, respectively. The abbreviations SmX$_1$*, SmX$_2$*, and SmX$_3$* denote unidentified ordered chiral smectic phases.

3.2.3. X-ray Diffraction

 doi:10.20944/preprints202511.0407.v1

To corroborate the identification of the LC phases, the four LC fluorenone derivatives were analyzed using XRD. The XRD patterns are shown in Figure 8. In the SmC* phase of (*R*)-**1a**, the experimentally estimated layer spacing (*L*) is 29.8 Å (Figure 8a, upper). Because the shorter layer spacing than the theoretical molecular length (34.5 Å) of (*R*)-**1a** implies a tilt of the LC molecules relative to the layer normal in the LC structure, the XRD pattern is consistent with the SmC* phase. The presumed tilt angle was ~30°. The XRD patterns of (*R*)-**1a** at 80 °C (Figure 8a, bottom) indicated the emergence of an ordered smectic (SmX*) phase below 109 °C. The value of *L* in the SmX* phase was 29.1 Å. The wide-angle diffractions ($2\theta > 15°$) correspond to intralayer order. Therefore, the SmX* phase is likely a chiral smectic F (SmF*) or chiral smectic I (SmI*) phase [64,65]. In the case of (*R*,*R*)-**2a**, the value of *L* at 142 °C was calculated to be 31.6 Å, which is shorter than the extended molecular length of (*R*,*R*)-**2a** (36.4 Å), as calculated using molecular mechanics (MM) methods (Figure 8b, upper). Based on the phase transition sequence and results of the POM analysis, the interdigitated layer structure should be formed in the high-temperature smectic phase. In the second smectic phase at 125 °C, the experimental value of *L* is 30.7 Å, which is shorter than the theoretically calculated molecular length of (*R*,*R*)-**2a** (36.4 Å) (Figure 8b, middle). The molecules of (*R*,*R*)-**2a** should be tilted in the layer structure in the LC phase at 125 °C. The XRD pattern of (*R*,*R*)-**2a** at 125 °C (Figure 8b, middle) indicated the formation of a SmC* phase in the temperature range of 77–140 °C. In the XRD pattern of (*R*,*R*)-**2a** at 30 °C (Figure 8b, bottom), several weak diffraction peaks appeared in the wide-angle region. These wide-angle peaks correspond to intralayer order in the ordered smectic (SmX_1*) phase. The XRD pattern of (*R*,*R*)-**3a** at 180 °C (Figure 8c, upper) was consistent with the interdigitated-type SmA* structure, which is similar to the LC structure in the high-temperature smectic phase. At 180 °C, the layer spacing *L* was 32.1 Å, which is shorter than the calculated molecular length of (*R*,*R*)-**3a** (37.2 Å) by MM methods. After the cooling-induced phase transition, *L* was shortened to 30.5 Å (Figure 8c, middle), implying the formation of a SmC* tilted layer structure at 130 °C. The XRD profile at 50 °C (Figure 8c, bottom) shows several peaks originating from the layered structure, including wide-angle peaks, which indicate intramolecular order. The complex XRD pattern reflects the ordered smectic (SmX_1*) phase that appears below 98 °C. The XRD profile of compound (*R*,*R*)-**4a** featured fewer peaks (Figure 8d, upper). Since the layer spacing *L* (31.1 Å) at 110 °C is shorter than the theoretically calculated molecular length of (*R*,*R*)-**4a** (42.2 Å), the XRD pattern at 110 °C is consistent with the SmC* phase. By contrast, the XRD pattern at 35 °C indicated crystalline order below 92 °C (Figure 8d, bottom).

 doi:10.20944/preprints202511.0407.v1

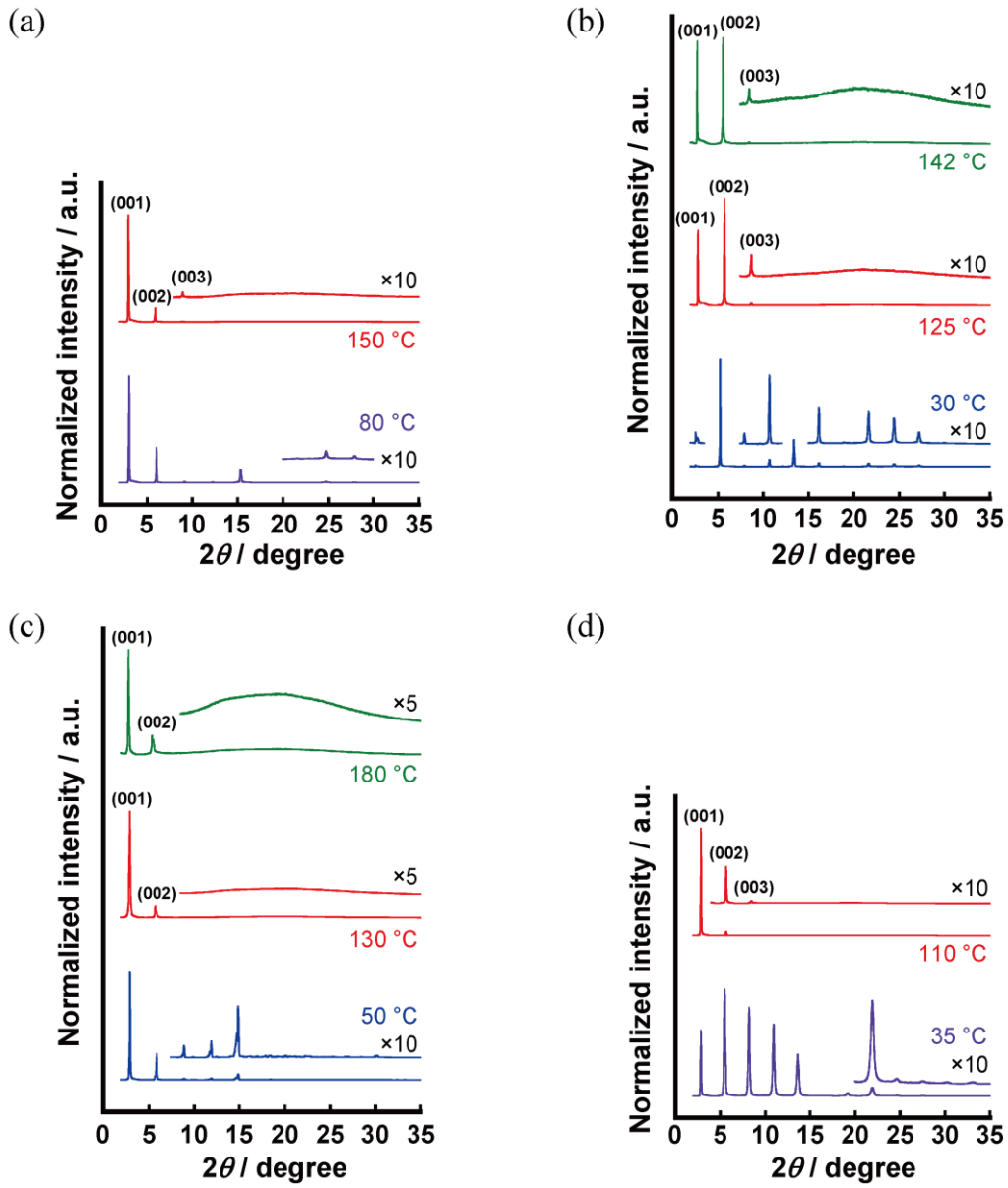

Figure 8. XRD patterns of (a) (*R*)-**1a**, (b) (*R*,*R*)-**2a**, (c) (*R*,*R*)-**3a**, and (d) (*R*,*R*)-**4a** at varying temperatures.

3.3. Ferroelectric Properties

We examined the ferroelectric properties of (*R*)-**1a**, (*R*,*R*)-**2a**, (*R*,*R*)-**3a**, and (*R*,*R*)-**4a**. All of these compounds exhibited ferroelectric hysteresis behavior in the SmC* phase (Figure 9). Although the spontaneous polarization (P_s) in the SmC* phase of (*R*,*R*)-**2a** reached 3.0 × 10^2 nC cm^{-2} at 110 °C, bilaterally asymmetric compound (*R*)-**1a** exhibited the lowest P_s among the four compounds (1.0 × 10^2 nC cm^{-2} at 150 °C). The P_s values for (*R*,*R*)-**2a** and (*R*,*R*)-**3a** were almost equal at 110 °C (~2.0 × 10^2 nC cm^{-2}). Comparing the P_s values for the ferroelectric π-conjugated LCs in our previous work [17,20,22], each compound showed a sufficiently large P_s in the SmC* phase. Furthermore, the P_s value for each chiral fluorenone derivative outperformed those of classical FLCs, such as chiral alkyl 4-*n*-alkyloxybiphenyl-4′-carboxylates (12–36 nC cm^{-2}) and chiral alkyl *N*-(4′-*n*-dodecyloxybenzylidene)-4-aminocinnamates (3–10 nC cm^{-2}) [66,67]. The electrical dipole of the central carbonyl unit in the fluorenone core probably contributed to the large P_s value. The fluorine groups on the wings should have also affected the ferroelectric polarization.

 doi:10.20944/preprints202511.0407.v1

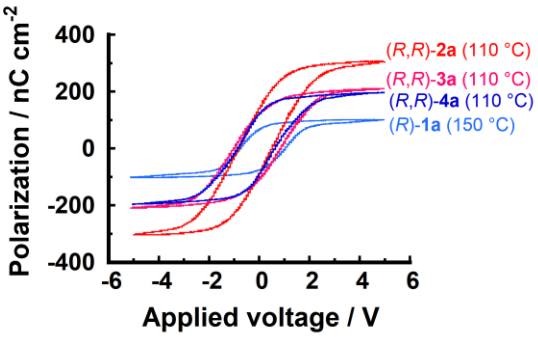

Figure 9. Polarization hysteresis loops of (*R*)-**1a**, (*R*,*R*)-**2a**, (*R*,*R*)-**3a**, and (*R*,*R*)-**4a** in the SmC* phases. The samples were planar oriented in 2 μm gap ITO cells. Triangular-wave bias was applied to the cells (±5 V, ±25 kV cm^{-1}, 100 Hz).

3.4. Carrier Transport Properties

The carrier transport properties of the LC phases of (*R*)-**1a**, (*R*,*R*)-**2a**, (*R*,*R*)-**3a**, and (*R*,*R*)-**4a** were evaluated using the time-of-flight technique and cells with 25 μm gaps. For each LC sample, transient photocurrent curves were measured for the positive and negative carriers in the SmC* phases (Figures 10, 11). The typical double logarithmic plots of the transient photocurrent curves for (*R*)-**1a** are displayed in Figure 10. In the photocurrent decays of (*R*)-**1a**, we found kink points that correspond to the transit times of the positive and negative carriers (Figure 8a,b). These transit times systematically shortened as the applied voltage increased from 120 to 200 V. The transient curves implied that the fluorenone-based FLC, (*R*)-**1a**, exhibited ambipolar carrier transport in the SmC* phase. While the mobility of positive carriers in the SmC* phases for (*R*)-**1a** reached ~6 × 10^{-5} cm^2 V^{-1} s^{-1} at 160 °C (+200 V), the mobility of negative carriers at the same temperature was determined to be 4 × 10^{-5} cm^2 V^{-1} s^{-1} (–200 V) from the transit times. The kink points also appeared in the photocurrent decays of each carrier in (*R*,*R*)-**2a** (Figure 11). Even in these two compounds, the transit time shortened with increasing applied voltage. The transient photocurrent profiles of (*R*,*R*)-**2a**, (*R*,*R*)-**3a**, and (*R*,*R*)-**4a** revealed ambipolar carrier transport in the SmC* phases of each compound. The mobilities of the positive and negative carriers in the FLC phase reached 10^{-5} cm^2 V^{-1} s^{-1}, which was on par with the hole and electron mobilities in the LC phases with loose π-stacks. Therefore, we considered that the transient photocurrent curves for the positive and negative carriers were attributed to hole and electron transport, respectively. In the SmC* phase of (*R*,*R*)-**2a**, the electron mobility was slightly higher than that of the holes (Table 2). Among the four fluorenone derivatives, the asymmetrically substituted fluorenone derivative (*R*)-**1a** showed the highest hole mobility in the SmC* phase. In addition to the thermal promotion of carrier hopping, the electron-donating thiophene unit containing a sulfur atom, which has a large atomic radius, probably contributed to improving the overlap of the molecular orbitals for the hole-conduction pathway. Comparing the electron mobilities in the SmC* phase, (*R*,*R*)-**2a** exhibited the highest mobility. As can be deduced from the XRD results, the (*R*,*R*)-**2a** molecules formed a relatively well-ordered layer structure in the SmC* phase among the four compounds. Therefore, the realization of significant orbital overlap between neighboring central fluorenone cores contributed to the high electron mobility.

 doi:10.20944/preprints202511.0407.v1

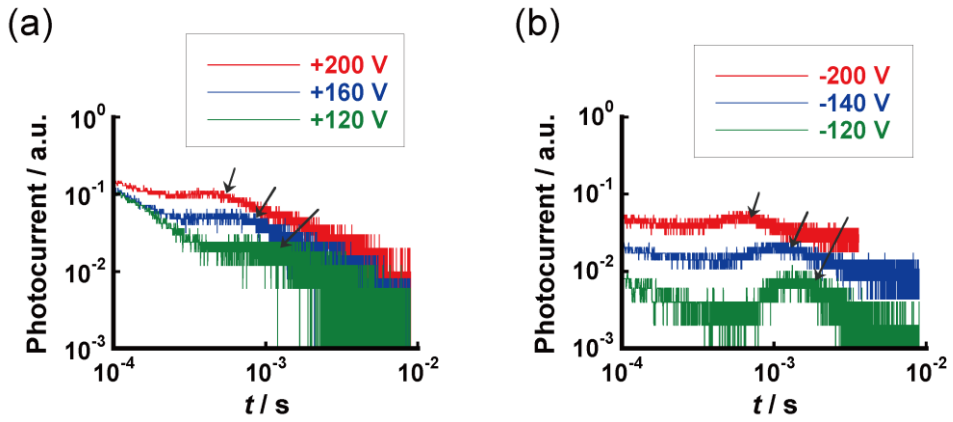

Figure 10. Double logarithmic plots of transient photocurrent curves for (a) positive and (b) negative carriers in the SmC* phase (160 °C) of (*R*)-**1a**. The black arrows in the plots indicate kink points corresponding to the transit times, that is, the time required for the charge carriers to reach the counter electrode.

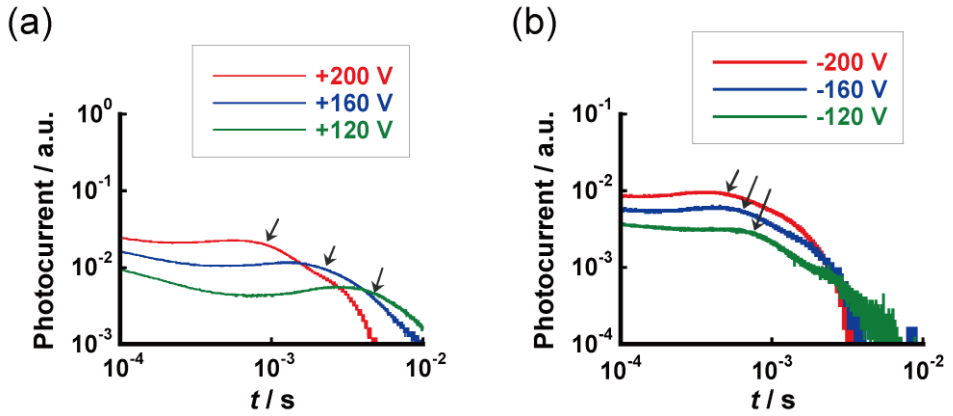

Figure 11. Double logarithmic plots of transient photocurrent curves for (a) positive and (b) negative carriers in the SmC* phase (120 °C) of (*R*,*R*)-**2a**. The black arrows in the plots indicate kink points corresponding to the transit times, that is, the time required for the charge carriers to reach the counter electrode.

Table 2. Carrier mobilities of chiral fluorenone derivatives.

Compound	*T* / °C	*V* / V	μ / cm² V⁻¹ s⁻¹ (Positive carrier)	*V* / V	μ / cm² V⁻¹ s⁻¹ (Negative carrier)
(*R*)-**1a**	160	+200	6×10^{-5}	−200	4×10^{-5}
(*R*,*R*)-**2a**	120	+200	3×10^{-5}	−200	6×10^{-5}
(*R*,*R*)-**3a**	130	+200	1×10^{-5}	−200	1×10^{-5}
(*R*,*R*)-**4a**	120	+200	1×10^{-5}	−200	1×10^{-5}

4. Conclusion

In this study, five chiral fluorenone derivatives were synthesized. Among them, only (*R*,*R*)-**2b** was a non-LC compound. The other fluorenone derivatives exhibited chiral smectic LC phases, including the SmC* phase. This indicates that the branched structure of the chiral chain strongly affected the emergence of LC phases in this system. The introduction of chiral (2-octyloxy)phenyl units on the 2- and 7-positions of the 9-fluorenone core promoted the formation of the SmA* structure. The dielectric polarization measurements revealed that (*R*)-**1a**, (*R*,*R*)-**2a**, (*R*,*R*)-**3a**, and (*R*,*R*)-**4a** exhibited ferroelectric behavior in their SmC* phases, with planar orientations in 2 μm thick LC cells. In particular, the fluorenone derivative (*R*,*R*)-**2a** exhibited the largest spontaneous polarization of the four compounds. The FLC fluorenone derivatives synthesized in this study exhibited ambipolar carrier transport in the SmC* phases. In their SmC* phases, the hole and electron mobilities were on

 doi:10.20944/preprints202511.0407.v1

the order of 10^{-5} cm^2 V^{-1} s^{-1}, which is on par with the carrier mobilities in the SmC and SmC* phases of conventional LC semiconductors. Although the hole mobility was slightly higher than the electron mobility in the SmC* phase of (*R*)-**1a**, the electron mobility was higher than the hole mobility in the SmC* phases of (*R*,*R*)-**2a**, (*R*,*R*)-**3a,** and (*R*,*R*)-**4a**. The UV–vis absorption spectra in dilute THF solution revealed that (*R*,*R*)-**4a** possessed the most favorable visible-light-absorption properties owing to the expansion of the π-conjugation system by the insertion of the ethynyl linker. We believe that these findings can inform the molecular design of novel ferroelectric π-conjugated LCs for the application of next-generation organic optoelectronic and electro-optic devices.

Supplementary Materials: The following supporting information can be downloaded at Preprints.org: Scheme S1: Synthesis of (*R*)-**1a**, (*R*,*R*)-**2a**, (*R*,*R*)-**2b**, (*R*,*R*)-**3a**, and (*R*,*R*)-**4a**; Figure S1: ^{1}H NMR spectrum of (*R*)-**1a**; Figure S2: ^{13}C NMR spectrum of (*R*)-**1a**; Figure S3: ^{1}H NMR spectrum of (*R*,*R*)-**2a**; Figure S4: ^{13}C NMR spectrum of (*R*,*R*)-**2a**; Figure S5: ^{1}H NMR spectrum of (*R*,*R*)-**2b**; Figure S6: ^{13}C NMR spectrum of (*R*,*R*)-**2b**; Figure S7: ^{1}H NMR spectrum of (*R*,*R*)-**3a**; Figure S8: ^{13}C NMR spectrum of (*R*,*R*)-**3a**; Figure S9: ^{1}H NMR spectrum of (*R*,*R*)-**4a**; Figure S10: ^{13}C NMR spectrum of (*R*,*R*)-**4a**; Figure S11: High-resolution ESI mass spectrum of (*R*)-**1a**; Figure S12: High-resolution ESI mass spectrum of (*R*,*R*)-**2a**; Figure S13: High-resolution ESI mass spectrum of (*R*,*R*)-**2b**; Figure S14: High-resolution ESI mass spectrum of (*R*,*R*)-**3a**; Figure S15: High-resolution ESI mass spectrum of (*R*,*R*)-**4a**.

Author Contributions: Conceptualization, A.S.; methodology, A.S.; validation, S.D., S.Y. and A.S.; formal analysis, S.D., S.Y. and A.S.; investigation, S.D., S.Y. and A.S.; resources, K.A. and A.S.; data curation, S.D., S.Y. and A.S.; writing—original draft preparation, S.D. and A.S.; writing—review and editing, A.S., S.D., S.Y. and K.A.; visualization, A.S. and S.D.; supervision, K.A. and A.S.; project administration, A.S.; funding acquisition, K.A. and A.S. All authors have read and agreed to the published version of the manuscript.

Funding: This study was financially supported by a Grant-in-Aid for Early-Career Scientists (No. 24K17746) from the Japan Society for the Promotion of Science (JSPS), and a Research Grant (2023, No.337) from the JKA, Japan, for A.S. This study was also financially supported by a research fund from the Tokyo University of Science for K.A. and A.S.

Data Availability Statement: Not applicable.

Acknowledgments: The authors thank Prof. Dr. M. Funahashi (Kobe University) for helping with electronic measurements, and Dr. Y. Yoshimura (Tokyo University of Science) for helping with HRMS measurements.

Conflicts of Interest: The authors declare no conflicts of interest.

References

1. Bisoyi, H. K.; Li, Q. Light-Directing Chiral Liquid Crystal Nanostructures: From 1D to 3D. *Acc. Chem. Res.* **2014**, *47*, 3184–3195.
2. Pescitelli, G.; Di Bari, L.; Berova, N. Application of electronic circular dichroism in the study of supramolecular systems. *Chem. Soc. Rev.* **2014**, *43*, 5211–5233.
3. Zhang, L.; Qin, L.; Wang, X.; Cao, H.; Liu, M. Supramolecular Chirality in Self-Assembled Soft Materials: Regulation of Chiral Nanostructures and Chiral Functions. *Adv. Mater.* **2014**, *26*, 6959–6964.
4. Yashima, E.; Ousaka, N.; Taura, D.; Shimomura, K.; Ikai, T.; Maeda, K. Supramolecular Helical Systems: Helical Assemblies of Small Molecules, Foldamers, and Polymers with Chiral Amplification and Their Functions. *Chem. Rev.* **2016**, *116*, 13752–13990.
5. Evers, F.; Aharony, A.; Bar-Gill, N.; Entin-Wohlman, O.; Hedegård, P.; Hod, O.; Jelinek, P.; Kamieniarz, G.; Lemeshko, M.; Michaeli, K.; Mujica, V.; Naaman, R.; Paltiel, Y.; Refaely-Abramson, S.; Tal, O.; Thijssen, J.; Thoss, M.; van Ruitenbeek, J. M.; Venkataraman, L.; Waldeck, D. H.; Yan, B.; Kronik, L. Theory of Chirality Induced Spin Selectivity: Progress and Challenges. *Adv. Mater.* **2022**, *34*, No.2106629.
6. Dierking, I. Chiral Liquid Crystals: Structures, Phases, Effects. *Symmetry* **2014**, *6*, 444–472.
7. Kitzerow, H.-S.; Bahr, C. (Eds.) *Chirality in Liquid Crystals*, 1st ed.; Springer: New York, USA, 2001.
8. Goodby, J. W. Symmetry and Chirality in Liquid Crystals. In *Handbook of Liquid Crystals*, 1st ed.; Demus, D.; Goodby, J. W.; Gray, G. W.; Spiess, H.-W.; Vill, V., Eds.; Wiley-VCH: Weinheim, Germany, 1998; Volume 1, pp. 115–132.
9. Meyer, R. B.; Libert, L.; Strzelecki, L.; Keller, P. Ferroelectric liquid crystals. *J. Phys.* **1975**, *36*, L69–L71.
10. Lagerwall, S. T.; Dahl, I. Ferroelectric Liquid Crystals. *Mol. Cryst. Liq. Cryst.* **1984**, *114*, 151–187.
11. Takanishi, Y.; Takezoe, H.; Suzuki, Y.; Kobayashi, I.; Yajima, T.; Terada, M.; Mikami, K. Spontaneous Enantiomeric Resolution in a Fluid Smectic Phase of a Racemate. *Angew. Chem., Int. Ed.* **1999**, *38*, 2353–2356.
12. Young, C. Y.; Pindak, R.; Clark, N. A.; Meyer, R. B. Light-Scattering Study of Two-Dimensional Molecular-Orientation Fluctuations in a Freely Suspended Ferroelectric Liquid-Crystal Film. *Phys. Rev. Lett.* **1978**, *40*, 773–776.

 doi:10.20944/preprints202511.0407.v1

13. Clark, N. A.; Lagerwall, S. T. Submicrosecond bistable electro-optic switching in liquid crystals. *Appl. Phys. Lett.* **1980**, 36, 899–901.
14. Lago-Silva, M.; Fernández-Míguez, M.; Rodríguez, R.; Quiñoá, E.; Freire. F. Stimuli-responsive synthetic helical polymers. *Chem. Soc. Rev.* **2024**, *53*, 793–852.
15. Zhang, M.; Kim, M.; Choi, W.; Choi, J.; Kim, D. H.; Liu, Y.; Lin, Z. Chiral macromolecules and supramolecular assemblies: Synthesis, properties and applications. *Prog. Polym.* **2024**, *151*, No. 101800.
16. García, F.; Gómez, R.; Sánchez, L. Chiral supramolecular polymers. *Chem. Soc. Rev.* **2023**, *52*, 7524–7548.
17. Seki, A.; Funahashi, M. Photovoltaic Effects in Ferroelectric Liquid Crystals based on Phenylterthiophene Derivatives. *Chem. Lett.* **2016**, *45*, 616–618.
18. Seki, A.; Funatsu, Y.; Funahashi, M. Anomalous photovoltaic effect based on molecular chirality: Influence of enantiomeric purity on the photocurrent response in π-conjugated ferroelectric liquid crystals. *Phys. Chem. Chem. Phys.* **2017**, *19*, 16446–16455.
19. Seki, A.; Funahashi, M. Chiral photovoltaic effect in an ordered smectic phase of a phenylterthiophene derivative. *Org. Electron.* **2018**, *62*, 311–319.
20. Seki, A.; Yoshio, M.; Mori, Y.; Funahashi, M. Ferroelectric Liquid-Crystalline Binary Mixtures Based on Achiral and Chiral Trifluoromethylphenylterthiophenes. *ACS Appl. Mater. Interfaces* **2020**, *12*, 53029–53038.
21. Seki, A.; Shimizu, K.; Aoki, K. Chiral π-Conjugated Liquid Crystals: Impacts of Ethynyl Linker and Bilateral Symmetry on the Molecular Packing and Functions. *Crystals* **2022**, *12*, No.1278.
22. Seki, A.; Funahashi, M.; Aoki, K. Ferroelectric Photovoltaic Effect in the Ordered Smectic Phases of Chiral π-Conjugated Liquid Crystals: Improved Current-Voltage Characteristics by Efficient Fixation of Polar Structure. *Bull. Chem. Soc. Jpn.* **2023**, *96*, 1224–1233.
23. Mulder, D. J.; Schenning, A. P. H. J.; Bastiaansen, C. W. M. Chiral-nematic liquid crystals as one-dimensional photonic materials in optical sensors. *J. Mater. Chem. C* **2014**, *2*, 6695–6705.
24. Hartmann, W. J. A. M. Ferroelectric Liquid Crystal Displays for Television Application. *Ferroelectrics* **1991**, *122*, 1–26.
25. Mondal, R.; Tönshoff, C.; Khon, D.; Neckers, D. C.; Bettinger, H. F. Synthesis, Stability, and Photochemistry of Pentacene, Hexacene, and Heptacene: A Matrix Isolation Study. *J. Am. Chem. Soc.* **2009**, *131*, 14281–14289.
26. Mushrush, M.; Facchetti, A.; Lefenfeld, M.; Katz, H. E.; Marks, T. J. Easily Processable Phenylene–Thiophene-Based Organic Field-Effect Transistors and Solution-Fabricated Nonvolatile Transistor Memory Elements. *J. Am. Chem. Soc.* **2003**, *125*, 9414–9423.
27. Wu, J. Polycyclic Aromatic Compounds for Organic Field-effect Transistors: Molecular Design and Syntheses. *Curr. Org. Chem.* **2007**, *11*, 1220–1240.
28. Fichou, D. Structural order in conjugated oligothiophenes and its implications on opto-electronic devices. *J. Mater. Chem.* **2000**, *10*, 571–588.
29. Zhang, L.; Colella, N. S.; Cherniawski, B. P.; Mannsfeld, S. C. B.; Briseno, A. L. Oligothiophene semiconductors: synthesis, characterization, and applications for organic devices. *ACS Appl. Mater. Interfaces* **2014**, *6*, 5327–5343.
30. Warman, J. M.; de Haas, M. P.; Dicker, G.; Grozema, F. C.; Piris, J.; Debije, M. G. Charge Mobilities in Organic Semiconducting Materials Determined by Pulse-Radiolysis Time-Resolved Microwave Conductivity: π-Bond-Conjugated Polymers versus π−π-Stacked Discotics. *Chem. Mater.* **2004**, *16*, 4600–4609.
31. Pisula, W.; Zorn, M.; Chang, J. Y.; Müllen, K.; Zentel, R. Liquid Crystalline Ordering and Charge Transport in Semiconducting Materials. *Macromol. Rapid Commun.* **2009**, *30*, 1179–1202.
32. O'Neill, M.; Kelly, S. M. Ordered Materials for Organic Electronics and Photonics. *Adv. Mater.* **2011**, *23*, 566–584.
33. Funahashi, M. Nanostructured liquid-crystalline semiconductors – a new approach to soft matter electronics. *J. Mater. Chem. C* **2014**, *2*, 7451–7459.
34. Funahashi, M.; Kato, T. Design of liquid crystals: from a nematogen to thiophene-based π-conjugated mesogens. *Liq. Cryst.* **2015**, *42*, 909–917.
35. Seki, A.; Funahashi, M. Nanostructure Formation Based on the Functionalized Side Chains in Liquid-Crystalline Heteroaromatic Compounds. *Heterocycles* **2016**, 92, 3–30.
36. Kato, T.; Yoshio, M.; Ichikawa, T.; Soberats, B.; Ohno, H.; Funahashi, M. Transport of ions and electrons in nanostructured liquid crystals. *Nat. Rev. Mater.* **2017**, *2*, No.17001.
37. Funahashi, M.; Hanna, J. Photoconductive Behavior in Smectic A Phase of 2-(4'-Heptyloxyphenyl)-6-Dodecylthiobenzothiazole. *Jpn. J. Appl. Phys.* 1996, 35, No. L703.
38. Funahashi, M.; Hanna, J.-I. High Carrier Mobility up to 0.1 $cm^2 V^{-1} s^{-1}$ at Ambient Temperatures in Thiophene-Based Smectic Liquid Crystals. *Adv. Mater.* **2005**, *17*, 594–598.
39. Funahashi, M.; Sonoda, A. High electron mobility in a columnar phase of liquid-crystalline perylene tetracarboxylic bisimide bearing oligosiloxane chains. *J. Mater. Chem.* **2012**, *22*, 25190–25197.
40. Adam, D.; Closs, F.; Frey, T.; Funhoff, D.; Haarer, D.; Ringsdorf, H.; Schuhmacher, P.; Siemensmeyer, K. Transient photoconductivity in a discotic liquid crystal. *Phys. Rev. Lett.* **1993**, *70*, 457–460.

 doi:10.20944/preprints202511.0407.v1

41. Boden, N.; Bushby, R. J.; Clements, J.; Movaghar, B.; Donovan, K. J.; Kreouzis, T. Mechanism of charge transport in discotic liquid crystals. *Phys. Rev. B: Condens. Matter Mater. Phys.* **1995**, *52*, 13274–13280.
42. Simmerer, J.; Glüsen, B.; Paulus, W.; Kettner, A.; Schuhmacher, P.; Adam, D.; Etzbach, K.-H.; Siemensmeyer, K.; Wendorff, J. H.; Ringsdorf, H.; Haarer, D. Transient photoconductivity in a discotic hexagonal plastic crystal. *Adv. Mater.* **1996**, *8*, 815– 819.
43. Ban, K.; Nishikawa, K.; Ohta, K.; van de Craats, A. M.; Warman, J. M.; Yamamoto, I.; Shirai, H. Discotic liquid crystals of transition metal complexes 29: Mesomorphism and charge transport properties of alkylthiosubstituted phthalocyanine rare-earth metal sandwich complexes. *J. Mater. Chem.* **2001**, *11*, 321–331.
44. Demenev, A.; Eichhorn, S. H.; Taerum, T.; Perepichka, D. F.; Patwardhan, S.; Grozema, F. C.; Siebbeles, L. D. A.; Klenkler, R. Quasi temperature independent electron mobility in hexagonal columnar mesophases of an H-bonded benzotristhiophene derivative. *Chem. Mater.* **2010**, *22*, 1420–1428.
45. Pisula, W.; Menon, A.; Stepputat, M.; Lieberwirth, I.; Kolb, U.; Tracz, A.; Sirringhaus, H.; Pakula, T.; Mullen, K. A Zone Cast-ing Technique for Device Fabrication of Field-Effect Transistors Based on Discotic Hexa-peri-Hexabenzocoronene. *Adv. Mater.* **2005**, *17*, 684–689.
46. van Breemen, A. J. J. M.; Herwig, P. T.; Chlon, C. H. T.; Sweelssen, J.; Schoo, H. F. M.; Setayesh, S.; Hardeman, W. M.; Martin, C. A.; de Leeuw, D. M.; Valeton, J. J. P.; Bastiaansen, C. W. M.; Broer, D. J.; PopaMerticaru, A. R.; Meskers, S. C. J. Large Area Liquid Crystal Monodomain Field-Effect Transistors. *J. Am. Chem. Soc.* **2006**, *128*, 2336–2345.
47. Funahashi, M.; Zhang, F.; Tamaoki, N. High Ambipolar Mobility in a Highly Ordered Smectic Phase of a Dialkylphenylterthiophene Derivative That Can Be Applied to Solution-Processed Organic Field-Effect Transistors. *Adv. Mater.* **2007**, *19*, 353–358.
48. Mori, T.; Komiyama, H.; Ichikawa, T.; Yasuda, T. A liquid-crystalline semiconducting polymer based on thienylene–vinylene–thienylene: Enhanced hole mobilities by mesomorphic molecular ordering and thermoplastic shape-deformable characteristics. *Polym. J.* **2020**, *52*, 313–321.
49. Hassheider, T.; Benning, S. A.; Kitzerow, H. -S.; Achard, M. -F.; Bock, H. Color-Tuned Electroluminescence from Columnar Liquid Crystalline Alkyl Arenecarboxylates. *Angew. Chem. Int. Ed.* **2001**, *40*, 2060–2063.
50. Benning, S. A.; Oesterhaus, R.; Kitzerow, H. -S. Polarized electroluminescence of a discotic mesogenic compound. *Liq. Cryst.* **2004**, *31*, 201–205.
51. Aldred, M. P.; Contoret, A. E. A.; Farrar, S. R.; Kelly, S. M.; Mathieson, D.; O'Neill, M.; Tsoi, W. C.; Vlachos, P. A Full-Color Electroluminescent Device and Patterned Photoalignment Using Light-Emitting Liquid Crystals. *Adv. Mater.* **2005**, *17*, 1368–1372.
52. Hori, T.; Miyake, Y.; Yamasaki, N.; Yoshida, H.; Fujii, A.; Shimizu, Y.; Ozaki, M. Solution Processable Organic Solar Cell Based on Bulk Heterojunction Utilizing Phthalocyanine Derivative. *Appl. Phys. Express* **2010**, *3*, No. 101602.
53. Shin, W.; Yasuda, T.; Watanabe, G.; Yang, Y. S.; Adachi, C. Self-Organizing Mesomorphic Diketopyrrolo-pyrrole Derivatives for Efficient Solution-Processed Organic Solar Cells. *Chem. Mater.* **2013**, *25*, 2549–2556.
54. Kogo, K.; Maeda, H.; Kato, H.; Funahashi, M.; Hanna, J. Photoelectrical Properties of a Ferroelectric Liquid Crystalline Photoconductor. *Appl. Phys. Lett.* **1999**, *75*, 3348–3350.
55. Funahashi, M.; Hanna, J. High Ambipolar Carrier Mobility in Self-Organizing Terthiophene Derivative. *Appl. Phys. Lett.* **2000**, *76*, 2574–2576.
56. Funatsu, Y.; Sonoda, A.; Funahashi, M. Ferroelectric Liquid-crystalline Semiconductors Based on a Phenylterthiophene Skeleton: Effect of the Introduction of Oligosiloxane Moieties and Photovoltaic Effect. *J. Mater. Chem. C* **2015**, *3*, 1982–1993.
57. Yang, M.-C.; Hanna, J; Iino, H. Novel Calamitic Liquid Crystalline Organic Semiconductors Based on Electron-Deficient Dibenzo[c,h][2,6]naphthyridine: Synthesis, Mesophase, and Charge Transport Properties by the Time-of-Flight Technique. *J. Mater. Chem. C* **2019**, *7*, 13192–13202.
58. Porzio, W.; Destri, S.; Giovanella, U.; Pasini, M.; Motta, T.; Natali, D.; Sampietro, M.; Campione, M. Fluorenone–thiophene derivative for organic field effect transistors: A combined structural, morphological and electrical study. *Thin Solid Films* **2005**, *492*, 212–220.
59. Lincker, F.; Attias, A. -J.; Mathevet, F.; Heinrich, B.; Donnio, B.; Fave, J. -L.; Rannou, P.; Demadrille, R. Influence of polymorphism on charge transport properties in isomers of fluorenone-based liquid crystalline semiconductors. *Chem. Commun.* **2012**, *48*, 3209–3211.
60. Lim, C. J.; Lei, Y.; Wu, B.; Li, L.; Liu, X.; Lu, Y.; Zhu, F.; Ong, B. S.; Hu, X.; Ng, S. -C. Synthesis and characterization of two fluorenone-based conjugated polymers and their application in solar cells and thin film transistors. *Tetrahedron Lett.* **2016**, *57*, 1430–1434.
61. Suzuki, M.; Seki, A.; Yamada, S.; Aoki, K. Multi-stimuli-responsive behaviours of fluorenone-based donor–acceptor–donor triads in solution and supramolecular gel states. *Mater. Adv.* **2024**, *5*, 7401–7412.
62. Suzuki, M.; Yamada, S.; Iwai, K.; Aoki, K.; Seki, A. Acid vapor–responsive supramolecular gels of hydrogen-bonding D–A type fluorenones, *Chem. Lett.* 2025, *54*, No. upaf004.

 doi:10.20944/preprints202511.0407.v1

63. Kukhta, N. A.; da Silva Filho, D. A., Volyniuk, D.; Grazulevicius, J. V.; Sini, G. Can Fluorenone-Based Compounds Emit in the Blue Region? Impact of the Conjugation Length and the Ground-State Aggregation. *Chem. Mater.* **2017**, *29*, 1695–1707.
64. Rao, P. B.; Rao, N. V. S.; Pisipati, V. G. K. M. The Smectic F Phase in nO.m Compounds. *Mol. Cryst. Liq. Cryst.* **1991**, *206*, 9–15.
65. Ouchi, Y.; Uemura, T.; Takezoe, H.; Fukuda, A. Molecular Reorientation Process in Chiral Smectic I Liquid Crystal. *Jpn. J. Appl. Phys.* **1985**, *24*, 893–895.
66. Goodby, J. W. Optical Activity and Ferroelectricity in Liquid Crystals. *Science* **1986**, *231*, 350–355.
67. Kelly, S. M.; O'Neill, M. Liquid Crystals for Electro-Optical Applications. In *Handbook of Advanced Electronic and Photonic Materials and Devices. In Liquid Crystals, Display and Laser Materials*; H. S. Nalwa Ed.; Academic Press: New York, USA, 2001; Vol. 7, pp. 1−66.